Core-shell Ag_2CrO_4/N-GQDs@g-C_3N_4 composites with anti-photocorrosion performance for enhanced full-spectrum-light photocatalytic activities

Chengyang Feng[a,b], Yaocheng Deng[a,b], Lin Tang[a,b,*], Guangming Zeng[a,b,*], Jiajia Wang[a,b], Jiangfang Yu[a,b], Yani Liu[a,b], Bo Peng[a,b], Haopeng Feng[a,b], Jingjing Wang[a,b]

[a] College of Environmental Science and Engineering, Hunan University, Changsha, 410082, China
[b] Key Laboratory of Environmental Biology and Pollution Control, Hunan University, Ministry of Education, Changsha, 410082, China

ABSTRACT

It is a challenge to develop highly efficient and stable photocatalysts to harvest solar spectrum as broad as possible. In this work, for the first time, a nitrogen-doped graphene quantum dots (N-GQDs) modified Ag_2CrO_4@g-C_3N_4 core-shell structured composite was fabricated to achieve full-spectrum response from UV to near-infrared (NIR) region. In the Ag_2CrO_4/N-GQDs@g-C_3N_4 composites, Ag_2CrO_4 and g-C_3N_4 can be excited by UV and visible light, and N-GQDs can absorb NIR light to emit visible light, which greatly enhances the utilization of solar light. Moreover, compared with the normal hybrid heterojunctions, the core-shell structure provides larger contact area between Ag_2CrO_4 and g-C_3N_4. The large contact area and highly conductive N-GQDs effectively promote the photoelectron transfer from Ag_2CrO_4 to g-C_3N_4, which not only restrains the charge combination, but also greatly inhibits the photocorrosion of Ag_2CrO_4. The cycle experimental results showed that the performance of AN@CN did not decrease even after eight cycles of usage, and the XRD and EIS results also confirmed the stable nature of AN@CN composites. As a result, the optimized composites exhibit excellent photocatalytic degradation of doxycycline under full-spectrum light, and the possible photocatalytic mechanism was proposed. This work provides guidance for the design of high efficient photocatalysts with full-spectrum response and excellent stability.

1. Introduction

Facing two global challenges of environmental pollution and energy sources shortage, it is imperative to develop low-energy environmental restoration techniques [1–3]. In recent decades, the photocatalytic technology has been widely studied, which includes the degradation of organic pollutants [4,5], hydrogen production [6,7], CO_2 reduction [8,9], NO_x reduction [10,11] or ammonia synthesis [12], due to its environmental-friendly, low-energy and reusable properties. However, limited to the weak light response, serious charge recombination and poor stability, most photocatalysts are difficult for practical application. Therefore, many methods, such as element doping [13], compound modification [14] and introducing defects [15], are developed for photocatalysts's improvement, where the preparation of composite heterojunction is considered as the most convenient and efficient method. To date, several heterostructured photocatalysts (such as In_2S_3/$CdIn_2S_4$ [16], Bi_2O_3/Bi_2S_3/MoS_2 [17], CdS/Au/TiO_2 [18]; et al) have been reported. In the case of these heterojunction composites, normally, the photoexcited electrons and holes can shift to higher

conduction band (CB) and lower valance band (VB) respectively between different semiconductors, which greatly increase the efficiency of charge separation. In particular, when the band structure between composite semiconductors is suitable to form a Z-scheme heterojunction, the photoexcited electrons and holes can be kept at lower CB and higher VB and retain their redox potential.

g-C_3N_4 and Ag_2CrO_4 are two promising photocatalytic materials that have been widely studied, and both of them have advantages and disadvantages. The π-conjugated g-C_3N_4 is a well-known metal-free 2D material with excellent stability, simple preparation method and tunable morphology [19–23]. Serious charge recombination and poor electron transfer ability are two major problems that restrict the photocatalytic performance of g-C_3N_4 [24–26]. Ag_2CrO_4 exhibits superior optical absorption and electron conduction capability [27,28], but the severe photocorrosion makes it almost a disposable product. Considering that the VB and CB edge potential of Ag_2CrO_4 are located at about 2.16 eV and 0.38 eV respectively, which are very compatible with the band structure of g-C_3N_4 (VB = 1.64 eV, CB = −1.22 eV), the combination with reasonable structural design of Ag_2CrO_4 and g-C_3N_4
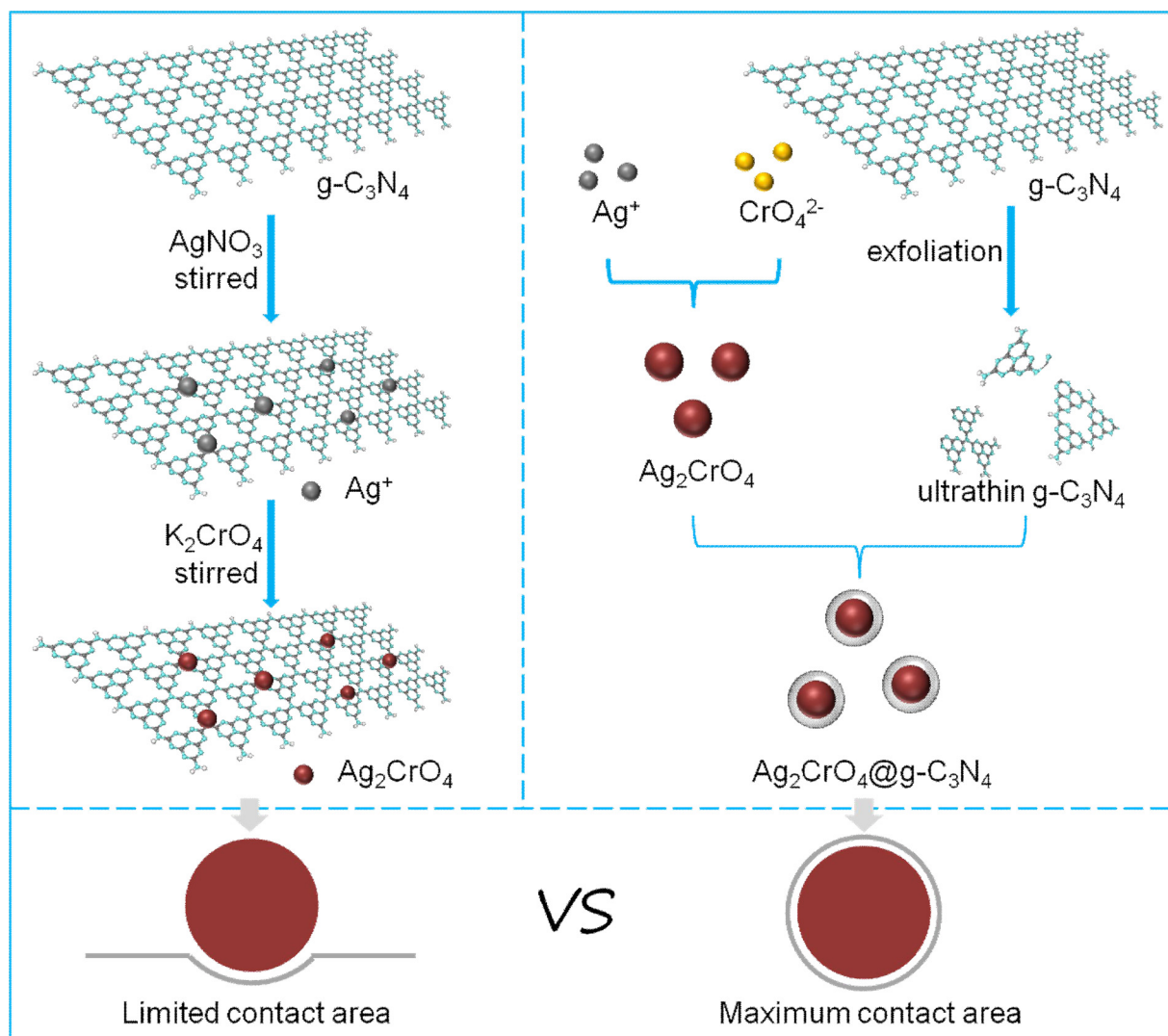
Scheme 1. The schematic diagram of combinations of Ag_2CrO_4 and $g-C_3N_4$. The growth of Ag_2CrO_4 nanoparticle on the surface of $g-C_3N_4$ obtain limited contact area, and the core-shell $Ag_2CrO_4@g-C_3N_4$ provide the maximum contact area.

are expected to exhibit with excellent photocatalytic performance, inhibited photocorrosion and reduced charge recombination. In our previous study, it was found that the growth of Ag_2CrO_4 on the surface of $g-C_3N_4$ can improve the efficiency of charge separation and inhibit photocorrosion to some extent [29]. Plenty of studies pointed out that the contact interface in heterojunction is the key to improve photocatalytic activity [30–32]. However, due to the limited contact area between $g-C_3N_4$ and Ag_2CrO_4 provided by the common hybrid growth method (Scheme 1), the charge transfer cannot be maximized. In order to maximize the contact area between $g-C_3N_4$ and Ag_2CrO_4, in this work, for the first time, a strategy to prepare core-shell $Ag_2CrO_4@g-C_3N_4$ was proposed. Herein, the ultrathin $g-C_3N_4$ via a concentrated H_2SO_4 exfoliation method [33,34] was obtained and attached to the Ag_2CrO_4 nanoparticles to form a core-shell structure.

Nitrogen-doped graphene quantum dots (N-GQDs), a novel type of nitrogen-doped carbon-based nanomaterials with dimensions below 10 nm, have attracted great attention in the field of high performance photocatalyst preparation due to its excellent electron transfer properties and unique up-conversion capacity [35,36]. Its excellent electron transfer property is often used to modify photocatalyst for better migration and separation of photo-charges [37]. Meanwhile, a series of studies have found that the photoresponse range of photocatalysts can be greatly expanded with the modification by N-GQDs. It was found

that the up-conversion effect of N-GQDs played an important role in these works, to convert long-wavelength near-infrared (NIR) light into available visible light [38]. Thus, to further improve the light utilization and charge separation, N-GQDs were introduced in the core-shell composites [36,38–40]. With the help of N-GQDs, NIR light, which accounts for more than 50% of solar lights and can't be used by most of photocatalysts, can be converted and utilized. The combination of these three materials can harvest solar spectrum from UV to NIR range, and achieve high solar energy utilization. Except for the up-conversion effect, it is proved that the electronic bridge effect of N-GQDs plays a positive role in the formation of Z-scheme heterojunction [37]. The existence of N-GQDs enhances the electron transfer capability of the interface between Ag_2CrO_4 and $g-C_3N_4$, and the transfer of photoelectrons from Ag_2CrO_4 to $g-C_3N_4$ is facilitated, which further inhibits the charge combination and photocorrosion.

The photocatalytic performances of prepared samples were evaluated by the degradation of doxycycline (DC) under UV, visible and NIR light, respectively. The AN@CN samples showed enhanced photocatalytic activities than pure $g-C_3N_4$ and Ag_2CrO_4 under both UV and visible light, and also attested with a certain degradation effect on DC under NIR light irradiation. Various characterizations and experiments were carried out to investigate the performance optimization and charge transfer mechanism of AN@CN. Based on the experimental
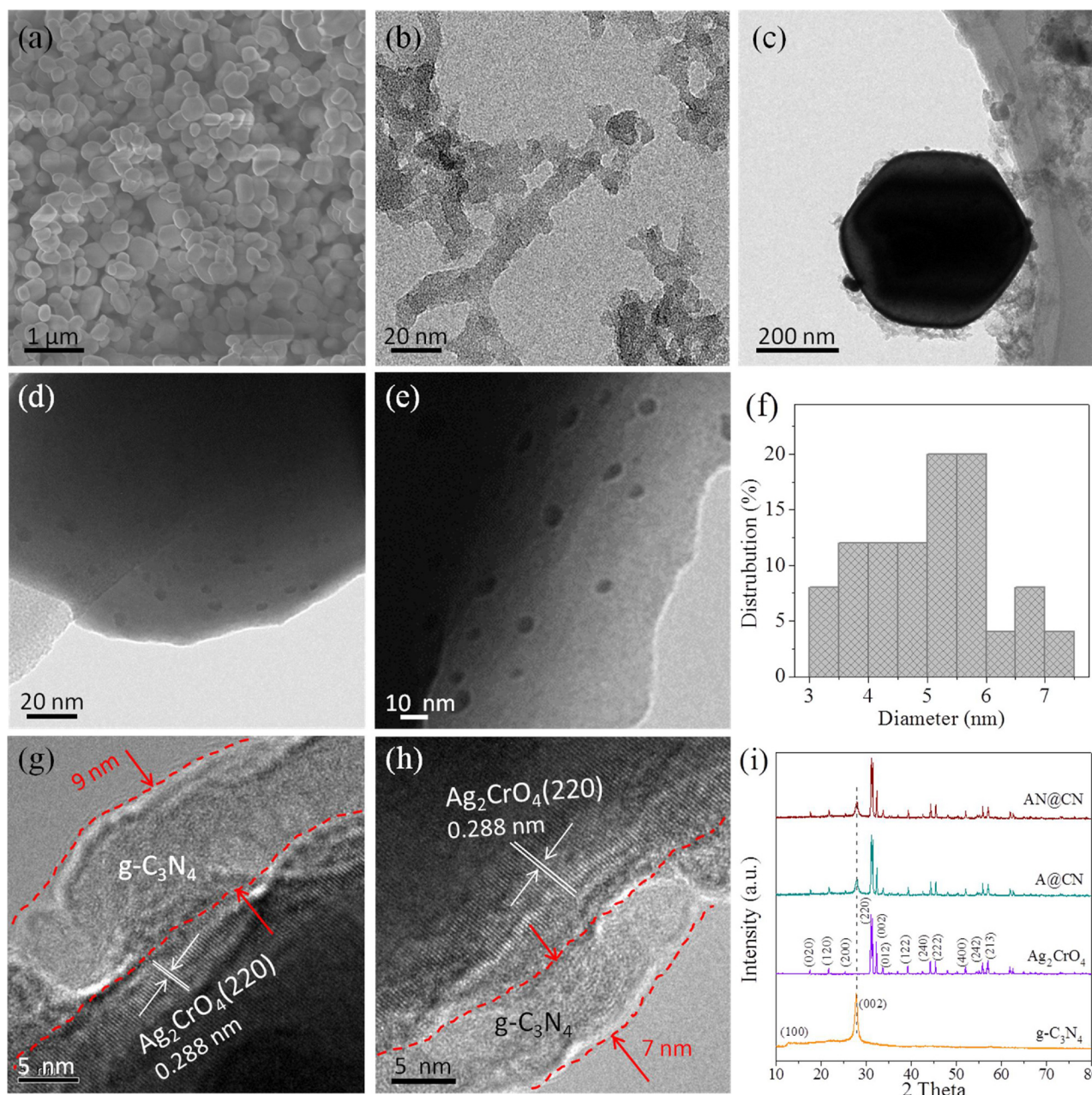
Fig. 1. (a) The SEM image of pure Ag_2CrO_4. (b) and (c) The TEM images of ultrathin g-C_3N_4 and AN@CN. (d–e) The TEM images and (f) particle size distribution of N-GQDs on Ag_2CrO_4. (g–h) The HRTEM images of core-shell structure of AN@CN. (i) XRD patterns of prepared samples.

results, a Z-scheme transfer mechanism was confirmed in the AN@CN composites, which significantly enhanced the charge separation and optical absorption, and inhibited the photocorrosion of Ag_2CrO_4.

2. Experimental section

2.1. Preparation of AN@CN core-shell photocatalysts

The preparation and optimization of AN@CN photocatalysts and associated diagrams are available in the supporting information.

2.2. Characterization of samples

The phase structures of as-prepared samples were examined by X-ray diffractometry (XRD) measurement on a Bruker AXS D8 Advances X-ray diffractometer with Cu-Kα irradiation (40 kV/40 mA). The surface properties were surveyed by Fourier-transform infrared spectroscopy (FTIR) and X-ray photoelectron spectroscopy (XPS) on an IR Prestige-21 spectrometer (using standard KBr disk method) and Thermo ESCALAB 250XI spectrometer (with Al Kα source), respectively. The morphologies were measured by a Hitachi S-4800 field emission scanning electron microscopy (FE-SEM, Hitachi, Japan), and the microstructures were investigated by a F20 S-TWIN transmission electron microscopy (TEM, Tecnai G2, FEI Co). The specific surface areas of obtained samples were characterized via a nitrogen adsorption-desorption and Brunauer-Emmett-Teller (BET) method by a surface area analyzer (NOVA 2200E, Quantachrome). The diffuse reflectance absorption spectra (DRS) of samples were obtained by a UV–vis spectrophotometer (Cary 300, USA) with an integrating sphere attachment, using $BaSO_4$ as the reference. The photoluminescence (PL) spectroscopy was measured by a Fluoromax-4 spectrofluorometer at room temperature.

2.3. Electrochemical measurements

The electrochemical and photoelectrochemical measurements were recorded by a CHI 660D workstation in a three-electrode cell with 0.1 M Na_2SO_4 electrolyte solution. A Pt electrode and an Ag/AgCl electrode were used as the counter and reference electrode, respectively, and FTO (active area of 1 cm^2) electrodes covered with samples were used as the working electrode. A 300 W Xe lamp was used as light source.

2.4. Photocatalytic tests

The photocatalytic activities of as-prepared samples were evaluated by the degradation of doxycycline (DC) under irradiation of full spectrum light. A 300 W Xe lamp with 420 nm and 760 nm cutoff filters was used as light source and located at a distance of 15 cm from the reaction device. In a typical procedure, 50 mg as-prepared catalyst was mixed with 100 mL DC solution (50 mg/L) and stirred for 30 min in the dark to achieve the adsorption-desorption equilibrium. During the irradiation, 5 mL reaction mixture was taken every 10 min and analyzed by UV–vis spectrophotometer. The concentrations of DC were further checked by high performance liquid chromatography (HPLC) (LC-20 AT, Shimadzu), which coupled with an Inert Sustain C18 column (4.6 × 250 nm, 5 µm particle size) and a L-2420 UV–vis detector set at 274 nm. The mobile phase was a mixture of 30% acetonitrile and 70% water (with 0.1% formic acid), at a flow rate of 1.0 mL/min. The sampleinjection volume was 10 µL and the column temperature was fixed at 25 °C. The used catalyst was collected by filtration and used for another run to test the stability. The temperature of reaction system was kept at 25 °C by a cryostat during the irradiation process.

2.5. Density-function-theory (DFT) calculations

The first-principles calculations were performed within the framework of DFT as implemented in the Vienna Ab-initio Simulation Package (VASP). The exchange-correlation interactions were treated by generalized gradient approximation (GGA) parameterized by Perdew, Burke, and Ernzerhof (PBE). The interaction between ions and electrons was described using the projected augmented wave (PAW) formalism with an energy cutoff of 400 eV. All the structures were fully relaxed until the force on each atom was less than 0.01 eV/Å. The Gaussian smearing was used with a smearing width of 0.2 eV. The Brillouin zone integrations were performed using Monkhorst-Pack scheme with 5 × 5 × 2 k-point mashes.

3. Results and discussion

3.1. Formation of AN@CN core-shell photocatalysts

The morphologies and nanostructure of prepared samples were investigated by SEM and TEM. Ag_2CrO_4 nanoparticles with uniform grain size about 400 nm could be observed in Fig. 1a. Fig. 1b shows the TEM image of ultrathin g-C_3N_4 nanosheets. After exfoliation, the g-C_3N_4 was cut into strip-like ultrathin nanosheets of about 10 nm wide, which was advantageous to the formation of g-C_3N_4 shell on the surface of Ag_2CrO_4. The N-GQDs were observed with evenly distribution on the surface of the Ag_2CrO_4 nanoparticles (Fig. 1d and e), and exhibited in relatively uniform size (Fig. 1f) with the diameter around 3 ~ 6 nm. The HRTEM images (Fig. S2a-c) clearly displayed the crystalline structure of N-GQDs, with lattice spacing of 0.20 nm, which matched well with the (101) lattice planes of graphite. Although the shell structure of g-C_3N_4 was too thin to be clearly observed in the low-magnification TEM image (Fig. 1c), it can be determined that the g-C_3N_4 is tightly wrapped on the surface of Ag_2CrO_4 in the HRTEM images (Fig. 1g and h). The core with a distinct lattice spacing of 0.288 nm stemmed from the exposed (220) planes of Ag_2CrO_4, and the amorphous shell was formed by the stacking of g-C_3N_4 nanosheets. From Fig. S2d-f, the N-GQDs could be observed

on the surface of Ag_2CrO_4 core and covered by g-C_3N_4 shell, indicating the successful preparation of the ternary core-shell AN@CN composites. The single and regular lattice indicated the well crystallization of Ag_2CrO_4. Comparing with the common compound mode, the core-shell structure provides larger contact area between Ag_2CrO_4 and g-C_3N_4, which was beneficial to the charge transfer between the two compositions, and furthermore, the high stable g-C_3N_4 shell could prevent the external corrosive substances from contacting the Ag_2CrO_4 core. The crystal and phase structure of prepared samples were identified by XRD as shown in Fig. 1i. Two diffraction peaks corresponding to the (100) interplanar packing of hepazine units and (002) π-π interlayer stacking structure (JCPDS 50-1250) could be observed at 12.7° and 27.8° on the XRD pattern of pure g-C_3N_4 [41–43]. The pure Ag_2CrO_4 exhibits twelve distinct diffraction peaks and can be identified as orthorhombic phase (JCPDS 26-0952). The strongest diffraction peak at 31.1° belongs to the (220) plane which can be observed in the HRTEM images (Fig. 1g and h). Apparently, all the major peaks of Ag_2CrO_4 and g-C_3N_4 were preserved after the formation of A@CN and AN@CN without impurity, demonstrating that the combination of the materials was successful, and the compound process would not destroy the crystal structure of Ag_2CrO_4. The specific surface areas of Ag_2CrO_4, g-C_3N_4, Ag_2CrO_4/N-GQDs and AN@CN were determined by nitrogen adsorption-desorption isotherm analysis. As shown in Fig. S3, all samples presented a type IV N_2 adsorption-desorption isotherms with the H3-type hysteresis loop. The BET specific surface areas of Ag_2CrO_4, g-C_3N_4, Ag_2CrO_4/N-GQDs and AN@CN samples were calculated to be 40.37, 231.92, 40.93 and 51.24 m^2/g, respectively. The introduction of N-GQDs has no obvious effect on the specific area of Ag_2CrO_4, due to the low amount of N-GQDs addition. And the specific area of composites increased after coating with g-C_3N_4, which could provide more reactive sites.

The element composition and chemical states of prepared samples along with the interfacial interaction between Ag_2CrO_4 and g-C_3N_4 were investigated by XPS measurements. The survey spectra (Fig. 2a) illustrated that the A@CN and AN@CN composites were composed of C, N, Ag, O and Cr, which was consistent with the sum of the elements contained in the g-C_3N_4 and Ag_2CrO_4. Fig. 2b showed the high resolution XPS of C 1s in g-C_3N_4, A@CN and AN@CN. The main peak located at 288.09 eV belonged to the C 1s in C=C–C bond [42], and the weak peak at 284.64 eV could be related to the carbon containing substances attached on the surface of the materials. Usually the absorbed carbon peak can be used as the standard peak for calibration of spectral graphs. And obviously, the peak at 284.64 got enhanced after the combination with Ag_2CrO_4 and introduction of N-GQDs, which can be attributed to the increased adsorption of carbonaceous substances during the preparation process. Meanwhile, a slight deviation of C 1s peak can be observed in A@CN and AN@CN (Fig. 2b), where the C 1s peak shifted to a higher binding energy position after combining with Ag_2CrO_4 and then shifted to a lower energy position after the introduction of N-GQDs. Similarly, the same shifting regularity was found in the main N 1s peak (C–N=C [44]) (Fig. 2c). However, Fig. 2e presented an opposite deviating phenomenon, where the peaks signal of Ag 3d, as compared with pure Ag_2CrO_4, shifted to lower binding energy in A@CN but moved to higher position in AN@CN. As displayed in Fig. 2d, the high resolution spectra of O 1s can be assigned to two peaks at around 530.04 eV and 531.59 eV. The gradually increased peak at 531.59 eV was attributed to the water species, oxygen and external −OH group adsorbed on the surface of prepared samples, and the peak at 530.04 eV was related to the crystal lattice oxygen of Ag_2CrO_4. In general, the shift of the XPS peaks after the combination of materials implies the change in electron density and is considered to be the evidence of the formation of heterojunction [45–47]. Concretely, the increased binding energy corresponds to the decreased electron density. Herein, the increased binding energy of C 1s and N 1s along with the decreased binding energy of Ag 3d in A@CN indicated that the electrons tended to transfer from g-C_3N_4 to Ag_2CrO_4, suggesting that a double-transfer heterojunction was formed in A@CN. But for AN@CN,
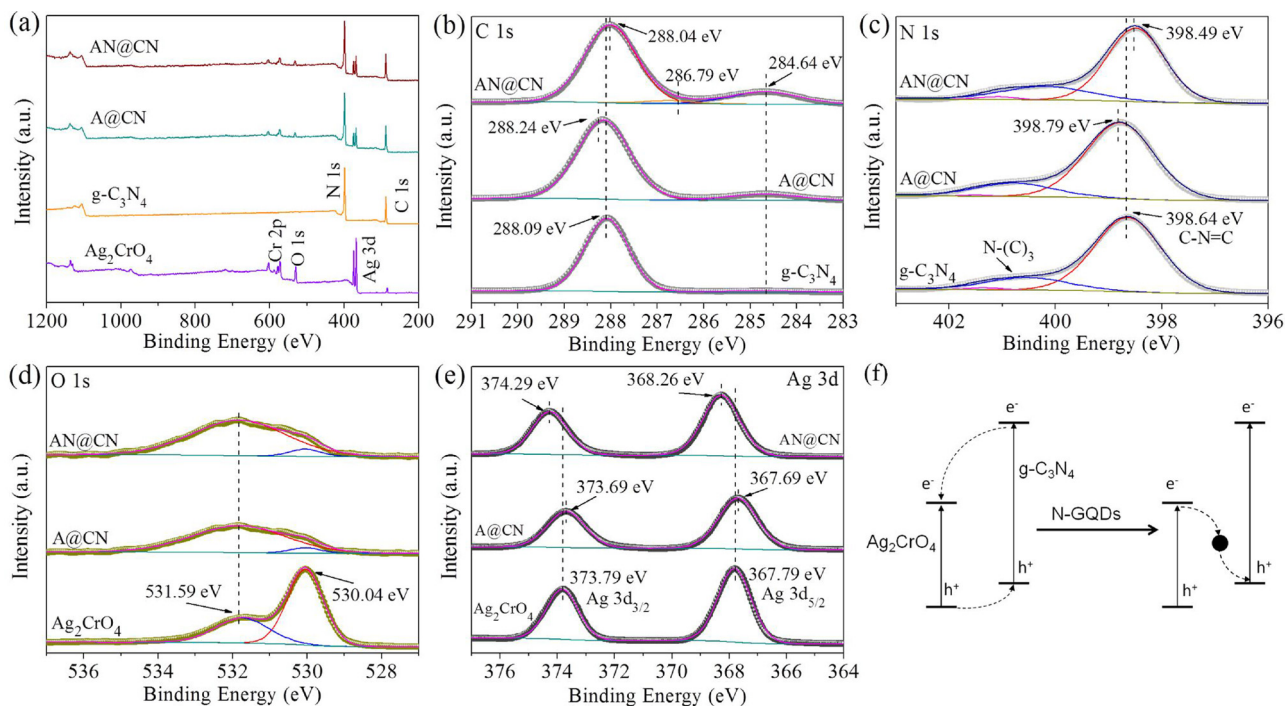
Fig. 2. (a) XPS survey spectra. High resolution XPS spectra of (b) C 1s, (c) N 1s, (d) O 1s and (e) Ag 3d. (f) The possible charge transfer mechanism in A@CN and AN@CN.

the reverse migration of peaks illustrated the increased electron density in g-C_3N_4 with the decreased electron density in Ag_2CrO_4, demonstrating the inverse electrons migration tendency from Ag_2CrO_4 to g-C_3N_4 after the introduction of N-GQDs. Hence, two charge transfer pathways could be put forward to account for the heterojunction type of A@CN and AN@CN (Fig. 2f). As for the A@CN, the electrons could shift from the CB of g-C_3N_4 to the CB of Ag_2CrO_4 and the holes could transfer from the VB of Ag_2CrO_4 to the VB of g-C_3N_4. After the introduction of N-GQDs, a Z-scheme transfer mechanism could be achieved in AN@CN composites. The introduced N-GQDs were anchored at the interface between Ag_2CrO_4 core and g-C_3N_4 shell, which could serve as the electron transfer mediator and avail the electrons transfer from the VB of Ag_2CrO_4 to the CB of g-C_3N_4. Apart from the significantly enhanced charge separation of hybrid photocatalyst which could also be obtained by the double-transfer pathway, Z-scheme mechanism would not reduce the redox activity of photoexcited holes and electrons. More importantly, the photocorrosion of Ag_2CrO_4 can be effectively inhibited by leading the electrons into g-C_3N_4. The formation of Z-scheme mechanism in AN@CN could be further proved by follow-up experiments and characterizations.

3.2. Optimized optical absorption and photoelectric performance

The optical properties of prepared samples were analyzed by UV–vis DRS spectra (Fig. 3a). Obviously, all the samples possessed UV–vis light response ability. The absorption edge of pure g-C_3N_4 was located at around 460 nm, and the pure Ag_2CrO_4 exhibited a broad absorption in UV to Vis region with an absorption edge around 770 nm. After Ag_2CrO_4 was coated with g-C_3N_4 shell, the absorbance in visible region decreased, which might ascribe to the g-C_3N_4 shell that prevents visible light from radiating into the Ag_2CrO_4 core. But in contract to the pure Ag_2CrO_4 and g-C_3N_4, the absorption of A@CN and AN@CN in UV region got distinct increase, which could be attributed to the formation of heterojunction between Ag_2CrO_4 and g-C_3N_4. For A@CN and AN@CN composites, two distinct absorption steps were appeared, indicating that the composites exhibited both optical absorption properties of Ag_2CrO_4 and g-C_3N_4. And compared to A@CN, the AN@CN composites

showed an obviously enhanced absorption peak at around 570 nm due to the introduction of N-GQDs. In addition, the band gaps of prepared samples were calculated by Kubelke-Munk transformation [48,49]:

$$(\alpha h \nu)^{1/n} = A(h\nu - E_g) \tag{1}$$

where α represents the absorption coefficient; h represents the Plank constant; ν is the light frequency; A is a constant; E_g is the band gap of semiconductor. The value of n determined to be $1/2$ due to the direct band gap nature of both Ag_2CrO_4 and g-C_3N_4 [29,50]. The calculated band gaps of samples (Tauc plots) were showed in Fig. 3b. The bandgaps of Ag_2CrO_4 and g-C_3N_4 were estimated to be 1.78 eV and 2.86 eV, respectively, which were close to the known values in previous literatures [51,52]. It was noticed that there were two linear regimes in the Tauc plots of A@CN and AN@CN, which derived two E_g values between $E_g(Ag_2CrO_4)$ and $E_g(g-C_3N_4)$. The Mott-Schottky (MS) plots of g-C_3N_4 and Ag_2CrO_4 were measured under frequency of 1000 Hz in the dark to estimate the flat band potential (U_{fb}) and the p-n type nature (Fig. 3c). According to the x-intercept of linear regimes in MS plots, the U_{fb} of g-C_3N_4 and Ag_2CrO_4 were -1.03 V and 0.48 V vs SCE which were equal to -0.79 V and 0.72 V vs NHE (Normal Hydrogen Electrode), respectively. Clearly, both g-C_3N_4 and Ag_2CrO_4 showed the n-type nature due to their positive slop linear MS plots. In general, the CB of an n-type semiconductor [53–55] is considered to be 0~0.2 V lower than U_{fb}, which could be regarded as an approximation of CB potential. The VB edge position of g-C_3N_4 and Ag_2CrO_4 were further measured by XPS valence band spectra and displayed in Fig. 3d. The VB potentials of g-C_3N_4 and Ag_2CrO_4 were estimated to be 1.64 eV and 2.16 eV, respectively. The CB potentials of g-C_3N_4 and Ag_2CrO_4 can be calculated by the equations below using the data obtained above.

$$E_{CB} = E_{VB} - E_g \tag{2}$$

Thus, the CB of g-C_3N_4 and Ag_2CrO_4 were calculated to be -1.22 eV and 0.38 eV, respectively. In order to further study the band structure of prepared samples, the density-functional theory (DFT) calculations of the band structure and partial density of states (PDOS) were performed and displayed in Fig. S4. The calculated band structures of Ag_2CrO_4 and
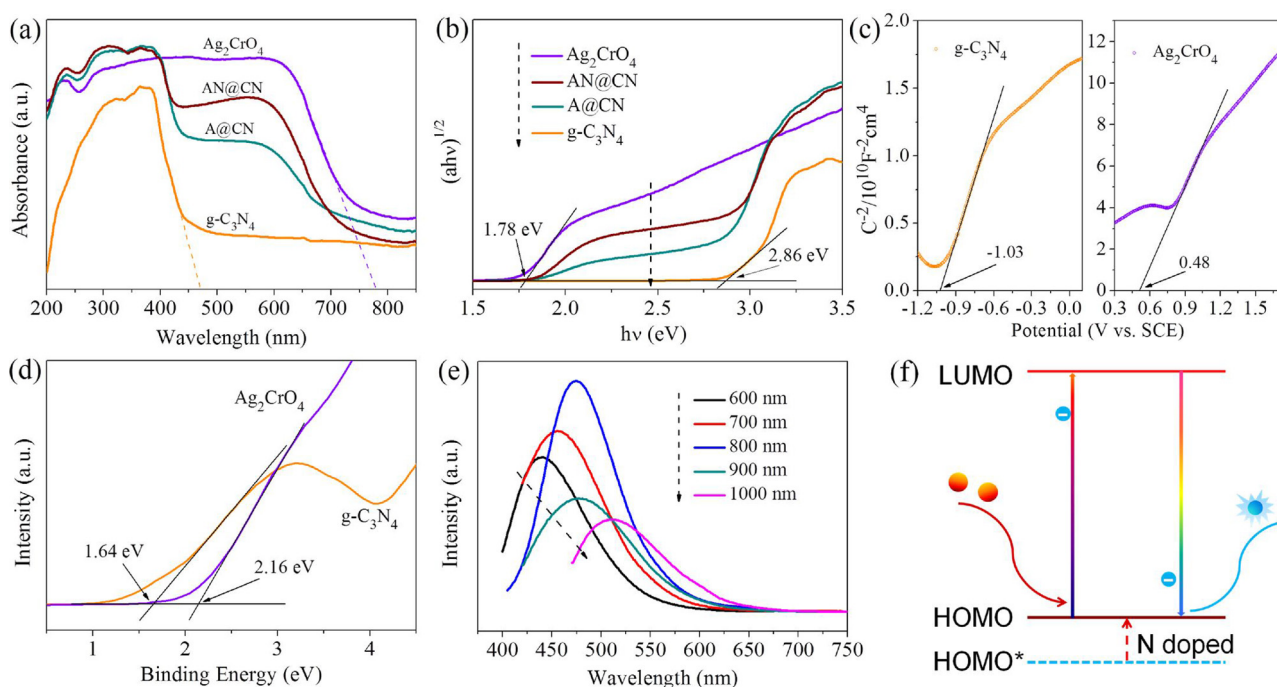
Fig. 3. (a) UV–vis DRS and (b) corresponding plots of transformed Kubelka-Munk function versus photon energy for g-C$_3$N$_4$, Ag$_2$CrO$_4$, A@CN and AN@CN. (c) The Mott-Schottky plot and (d) XPS valence band spectrum of g-C$_3$N$_4$ and Ag$_2$CrO$_4$. (e) Up-converted photoluminescence spectra of N-GQDs with excitation wavelengths from 600 to 1000 nm. (f) The mechanism of up-conversion effect of N-GQDs.

g-C$_3$N$_4$ (Fig. S4d-e) showed great matching for the formation of heterojunction. The negligible bandgap of N-GQDs (Fig. S4f) indicated its excellent electron transfer properties, which could accelerate the charge transfer between Ag$_2$CrO$_4$ and g-C$_3$N$_4$. The PDOS results (Fig. S4g-h) revealed that the VB of Ag$_2$CrO$_4$ was mainly composed of d-orbitals of Ag and p-orbitals of O atoms, while the CB was mainly constructed by d-orbitals of Cr atoms and small contributions of p-orbitals of O atoms. In the case of g-C$_3$N$_4$, the VB and CB were mainly constructed by p-orbitals of N and C atoms, respectively.

The up-converted PL spectra with excitation wavelengths from 600 to 1000 nm were measured to explore the up-conversion luminescence effect of N-GQDs. As shown in Fig. 3e, N-GQDs displayed up-conversion PL behavior to emit visible light around 425–520 nm with the excitation wavelengths from 600 to 1000 nm, and exhibited the strongest emitting light at around 475 nm with the excitation wavelength of 800 nm. The proposed mechanism of up-conversion effect of N-GQDs was illustrated in Fig. 3f. The up-conversion PL effect of N-GQDs belongs to a two-photon fluorescence process [38,56,57] based on the π-π electron transition in the large π-conjugated system, by which the N-GQDs can absorb two long wavelength photons to emit a higher energy photon with short wavelength. The doped nitrogen can facilitate the charge transfer in N-GQDs due to its electron donating effect. Furthermore, the strong electron donating effect of the doped nitrogen can elevate the primary HOMO* to a new higher HOMO and decrease the bandgap, which is conducive to the excitation of photogenerated electrons.

In order to verify the galvanizing impact by the existence of Ag$_2$CrO$_4$ and N-GQDs on the separation of photoexcited electrons and holes in g-C$_3$N$_4$, the PL spectra of Ag$_2$CrO$_4$, g-C$_3$N$_4$, A@CN and AN@CN were measured with an excitation wavelength of 320 nm and displayed in Fig. 4a. The pure g-C$_3$N$_4$ owning serious charge recombination nature emerged with very strong PL intensity, which drastically reduced after the combination with Ag$_2$CrO$_4$, manifesting that the interaction between g-C$_3$N$_4$ and Ag$_2$CrO$_4$ can significantly enhance the charge separation rate of g-C$_3$N$_4$. Analogously, the introduction of N-GQDs could also enhance the charge separation to some extent due to

its electron bridge effect, and the PL peak further decreased after the introduction of N-GQDs. In general, the change of electrochemical impedance spectroscopy (EIS) is related to the interfacial properties of materials. In heterojunction materials, the presence of built-in electric field on the contact interface can promote the migration and separation of photogenerated charges on different semiconductors, and the intuitive manifestation of the phenomenon is the reduction of impedance [51,52,58]. As shown in Fig. 4b, the arc radius on the EIS Nyquist plots reflects the electron transfer resistance of materials, where the AN@CN showed the best electron transfer ability under visible light compared with g-C$_3$N$_4$, Ag$_2$CrO$_4$ and A@CN. In view of the conductivity related to the quantity of photoexcited electrons in semiconductors, the EIS results reflected from a different angle that the synergies among g-C$_3$N$_4$, Ag$_2$CrO$_4$ and N-GQDs can enhance the charge separation (increase the free electron quantity) of AN@CN. The photocurrent transient response curves of prepared samples (Fig. 4c) further indicated the success of the charge separation promotion strategy in this work. The A@CN showed the enhanced photocurrent response compared with pure g-C$_3$N$_4$ or Ag$_2$CrO$_4$. Moreover, the AN@CN showed the strongest photocurrent response among all samples. The photocurrent of AN@CN under near-infrared light (λ > 760 nm) was also measured and showed in Fig. 4d to validate the near-infrared light excited ability. Although the photocurrent intensity of AN@CN under near-infrared light (about a quarter of which under visible light) was not strong enough, it was proved with good stability. Additionally, it manifested that the N-GQDs could do turn the long wavelength light into short wavelength for g-C$_3$N$_4$ and Ag$_2$CrO$_4$, providing the possibility for the utilization of full-spectrum sunlight.

Apart from the optical absorption ability and charge separation rate, the efficiency of charge injection yield to the electrolyte also plays a crucial role in controlling the reaction efficiency. The surface transfer efficiency (η_t) can be roughly obtained through a series of clever photoelectrochemical tests [59–62]. Briefly, the photocurrent of g-C$_3$N$_4$ and AN@CN were measured in 0.1 M Na$_2$SO$_4$ electrolyte solution, and the enhanced photocurrent curves were obtained by adding H$_2$O$_2$ to scavenge the photo-electrons. The test results were displayed in Fig. S5,
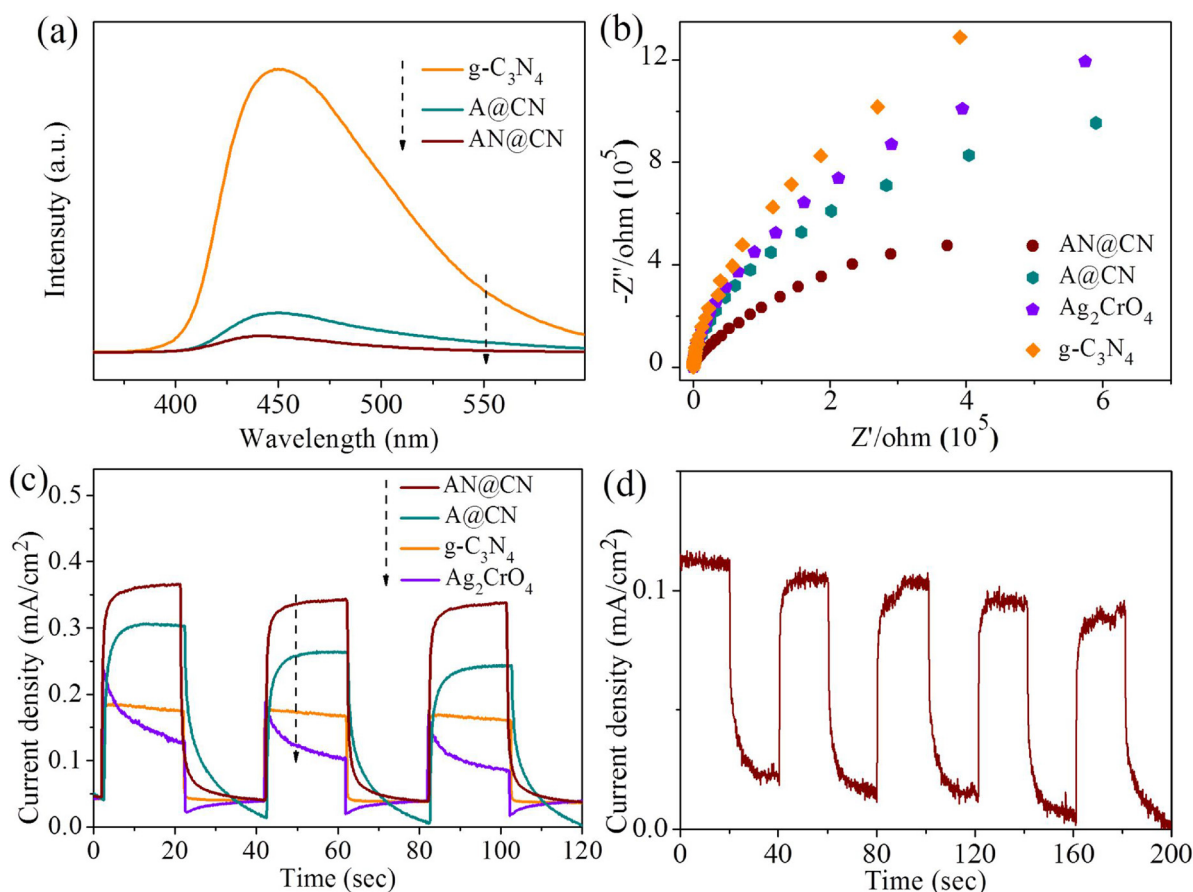
Fig. 4. (a) Photoluminescence spectra (PL) of g-C$_3$N$_4$, Ag$_2$CrO$_3$, A@CN and AN@CN with an excitation wavelength of 320 nm; (b) Electrochemical impedance spectroscopy (EIS) and (c) transient photocurrent density of g-C$_3$N$_4$, Ag$_2$CrO$_3$, A@CN and AN@CN under visible light (λ > 420 nm) irradiation; (d) Transient photocurrent density of AN@CN under near-infrared light (λ > 760 nm) irradiation.

and the photocurrent density can be defined by the following Eq. (3):

$$J_p = J_a \times \eta_s \times \eta_t \qquad (3)$$

where J_p is the photocurrent density in electrolyte, J_a is the photocurrent density converted by the absorbed photo energy, η_s is the charge separation efficiency, η_t represent the surface transfer efficiency.

As the electron scavenger H$_2$O$_2$ can increase the surface transfer efficiency (η_t) to almost 100%, the photocurrent density in the presence of H$_2$O$_2$ can be defined by the following equation (4):

$$J_P^{H2O2} = J_a \times \eta_s \qquad (4)$$

where J_a and η_s are unchanged for both g-C$_3$N$_4$ and AN@CN with or without H$_2$O$_2$, so the surface transfer efficiency (η_t) can be achieved based on equation (3) and (4):

$$\eta_t = J_p / J_P^{H2O2} \qquad (5)$$

Thus, the surface transfer efficiency (η_t) of g-C$_3$N$_4$ and AN@CN can be calculated using the data in Fig. S5a and b to be 30.7% and 47.4%, respectively. The higher surface charge transfer efficiency of AN@CN manifests that it's more favorable to inject the electrons into solution for reaction, which might ascribe to the increased surface electron density testified by the XPS analysis above.

3.3. Photocatalytic performance

The photocatalytic activities of as-prepared photocatalysts were investigated by degrading DC (50 mg/L) aqueous solution under UV (< 420 nm), visible (> 420 nm) and near-infrared (> 760 nm) light irradiation, which were presented in Fig. 5a–c where the inserted images

corresponded to the reaction kinetic analysis. Pure g-C$_3$N$_4$ and Ag$_2$CrO$_4$ showed limited activities due to their serious recombination of photogenerated electrons and holes. Benefiting from the enhanced charge separation after the formation of Ag$_2$CrO$_4$/g-C$_3$N$_4$ binary heterojunction, the degradation rate of A@CN significantly enhanced. However, neither pure catalysts nor binary heterojunction can degrade DC under near-infrared light. The wide band gap has a serious effect on the absorption of long wavelength light and limits the full use of solar energy. Fortunately, as expected, after the introduction of N-GQDs, the AN@CN showed incremental catalytic performance under near-infrared light with DC removal about 39.9% after 120 min. Although the effect was still general, the utilization rate of sunlight was improved to a certain extent. Additionally, benefitting from the enhanced charge separation rate, the increased surface electron density and the improved photoresponsiveness, the AN@CN showed the maximum degradation speed of DC under all light conditions. In order to eliminate the influence of adsorption effect on the experiment data, the adsorption tests of as-prepared samples for DC were carried out in the dark conditions. As illustrated in Fig. 5d, all the samples showed a similar adsorption performance of about 4% ∼ 8%, which is much lower than the degradation rate and won't affect the accuracy of the experimental results. The degradation process of DC was preliminary studied by UV–vis spectrophotometry and shown in Fig. S6. The spectrum of original DC solution exhibited two main peaks at 273.7 nm and 344.8 nm with a valley at 233.6 nm. As the reaction progressed, both the two main peaks gradually decreased proving the degradation of DC. However, the absorbance at the valley increased obviously within the first 40 min and then became decreased. The increased absorbance of valley indicated the generation of intermediate products, and the subsequent overall
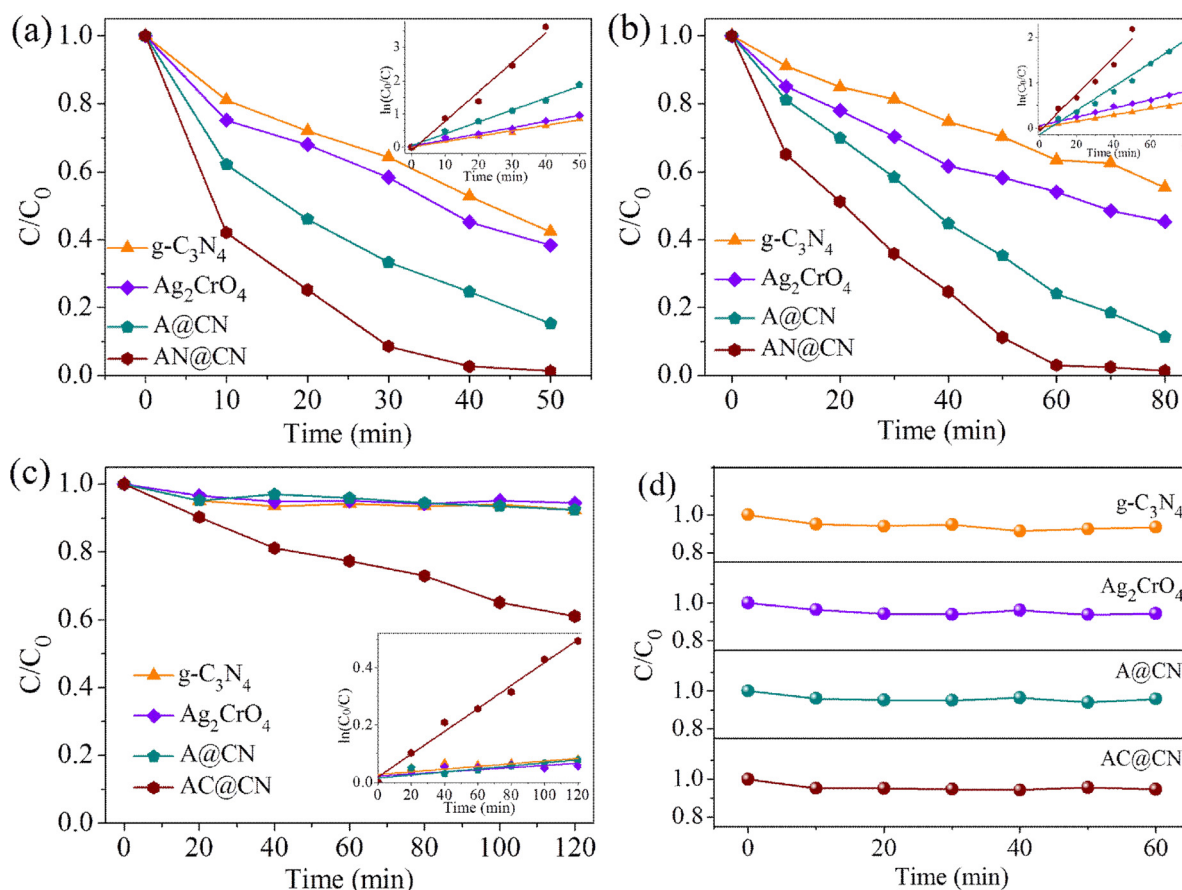
Fig. 5. Photocatalytic activities of as-prepared samples under (a) UV light, (b) visible light and (c) near-infrared light. Inset: the corresponding reaction kinetic curves. (d) Adsorption effect of as-prepared samples toward DC in dark.

decline demonstrated its degradation with further mineralization. In order to visually demonstrate the superior performance of AN@CN, a comparison with other recently reported photocatalysts for the degradation of doxycycline and other tetracycline antibiotics was made in Table S2. Obviously, the AN@CN composite has a better photocatalytic performance. Compared with other materials, it takes less time and less dosage for AN@CN to achieve a higher degradation effect. In addition, the practical application of AN@CN under natural environmental was further investigated under the strong and weak natural light (Location: Hunan University, N28°11′14.26″ E112°57′6.17″; August 6, Sunny; September 2, Cloudy) and estimated by the corresponding degradation efficiency along with TOC removal rate. As presented in Fig. S7a conducted under strong natural light, although the intensity of natural light is weaker than that of Xe lamp, AN@CN still showed excellent degradation and mineralization capacity of DC with almost complete degradation in 180 min as well as the TOC removal rate of 34%. The photocatalytic performance of AN@CN under weak natural light was displayed in Fig. S7b. As the natural light was too weak on cloudy days, it took about 5 h to remove DC completely, and the TOC removal effect also dropped a lot, only about 20%. According to the experiment results, the prepared AN@CN photocatalysts not only showed excellent photocatalytic performance under strong natural light, but also could degrade DC under weak natural light irradiation, which endowed the possibility for the practical application in the natural environment. In order to test the universal applicability of AN@CN catalysts, two other common pollutants, tetracycline (TC) and Rhodamine B (RhB), were selected as target pollutants to measure the photocatalytic performance. As shown in Fig. S8, the AN@CN composites exhibited excellent degradation performance for both TC and RhB under visible light irradiation. The degradation rates of TC and RhB reached 95.3% and

84.7%, respectively, after one hour reaction. Moreover, the TOC removal rate of TC and RhB reached 61.6% and 47.3%, respectively, indicating the great mineralization capability of AN@CN photocatalysts. In conclusion, the prepared AN@CN photocatalysts exhibited good degradation performance to various pollutants under different light conditions, which reflects the wide application nature of the catalysts.

3.4. Stability and photocorrosion inhibition

To evaluate the stability of obtained photocatalysts, the Ag_2CrO_4 and AN@CN samples were used in cycling experiments. Briefly, the used photocatalysts were collected by filtration, washed, dried and then applied for another round of DC degradation under the same conditions. As shown in Fig. 6a, the photocatalytic activity of Ag_2CrO_4 significantly declined after five cycles, while the AN@CN samples still remained high reactivity even after eight cycles. The XRD pattern of recycled Ag_2CrO_4 and AN@CN were measured to investigate the causes of phenomenon in cycling experiments. Clearly in Fig. 6b, many peaks in the XRD pattern of used Ag_2CrO_4 shifted, decreased or disappeared compared to the fresh sample, especially for the two main peaks corresponding to the (200) and (002) planes of Ag_2CrO_4, indicating the damage of the crystallization of used Ag_2CrO_4. The lattice damage could be attributed to the reduction of silver by the accumulated photoexcited electrons on Ag_2CrO_4 in the reaction process. However, as shown in Fig. 6c, the characteristic peaks of Ag_2CrO_4 in the XRD pattern of the recycled AN@CN were almost the same as the fresh one, indicating that the existence of g-C_3N_4 shell could significantly inhibit the photocorrosion of Ag_2CrO_4 core. In AN@CN, the photoelectrons excited on the CB of Ag_2CrO_4 would be transferred to the VB of g-C_3N_4, which
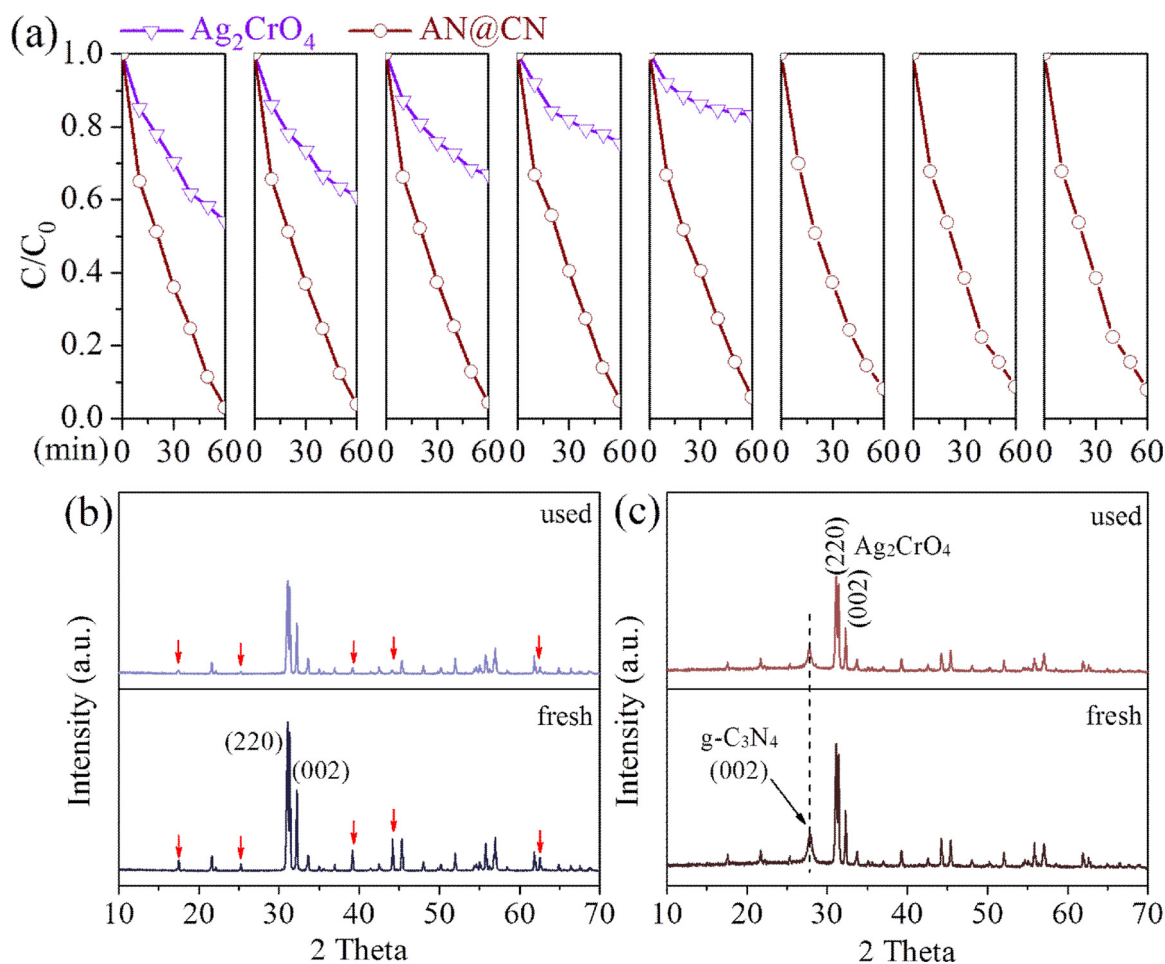
Fig. 6. (a) Cycling test of Ag_2CrO_4 and AN@CN under visible light irradiation. XRD patterns of the fresh and used (b) Ag_2CrO_4 and (c) AN@CN.

could be further reinforced by the electron bridge effect of N-GQDs. And compared with the fresh one, the characteristic peak of $g-C_3N_4$ (002) plane just showed a slight decline and still could be observed clearly after eight cycles, revealing the stable combination between Ag_2CrO_4 core and $g-C_3N_4$ shell. The EIS test was performed to investigate the changes in the conductivity of catalysts under visible light irradiation before and after used (Fig. S9). Obviously, the conductivity of Ag_2CrO_4 decreased sharply after five cycles, combined with XRD analysis results, it can be inferred that the damage of the crystallization caused by photocorrosion could inhibit the photoelectron transport and photoelectric response. The EIS pattern of AN@CN after 8 cycles was almost the same as the fresh one, indicating the unchanged photoelectric response and photoelectron transfer ability. The results demonstrated the excellent stability and photocorrosion inhibition of the prepared core-shell AN@CN photocatalysts.

3.5. Photocatalytic mechanism

To reveal the possible photocatalytic mechanism of AN@CN, active species trapping experiments were carried out to investigate the contributing active species during the degradation process. Fig. 7a shows the degradation curves over AN@CN with the addition of several scavengers. In the reaction system, ethylenediaminetetraacetic acid disodium (EDTA-2Na), isopropanol (IPA) and 1,4-benzoquinone (BQ) were used as scavengers for holes (h^+), hydroxyl radical (OH) and superoxide radical (O_2^-), respectively. Obviously, the photocatalytic performance of AN@CN was severely suppressed in the presence of EDTA-2Na, indicating the holes were the main active species in the reaction process. In addition, the degradation effect was also restrained

by BQ dramatically, confirming the contribution of O_2^- in DC degradation. However, the existence of IPA just caused a little inhibitory effect for AN@CN, which could be attributed to the fact that the VB of Ag_2CrO_4 and $g-C_3N_4$ are not high enough to generate OH. The TOC removal efficiency of AN@CN with different scavengers was also measured to intensive study the contribution of each active species to the reaction system (Fig. 7b). With the existence of EDTA-2Na, the TOC removal rate sharply declined from 36.6% to 1.2%, while the TOC removal rate just declined 11.8% in the presence of BQ. Based on the above experimental phenomena, the following inference can be proposed. Both h^+ and O_2^- are the dominated active species for the degradation of DC. However, only can h^+ have the ability to convert DC into H_2O and CO_2. O_2^- is not active enough to mineralize DC but just destroy its molecular structure. And a synergistic effect between h^+ and O_2^- could exist, where the pre-destroyed DC molecular by O_2^- could accelerate the mineralization process by the h^+. And this is why the TOC removal rate reduced after the addition of O_2^- scavengers (BQ). To further confirm the existence of O_2^-, the ESR (electron spin resonance) spin-trap technology based on $g-C_3N_4$ and AN@CN under visible light irradiation was performed. As shown in Fig. 7c, the characteristic signals of DMPO-O_2^- could be clearly observed for both the $g-C_3N_4$ and AN@CN samples, and the peak intensity of AN@CN is much higher than $g-C_3N_4$ (about triple of it), indicating the enhanced O_2^- generation ability of AN@CN. Combining with the previous characterization and experiment, the superior O_2^- generation ability could be attributed to the enhanced optical absorption, charge separation and surface electron transfer efficiency after the formation of AN@CN coreshell structure. Given that in ordinary double transfer heterojunction, the photoelectrons will shift from the semiconductor with high
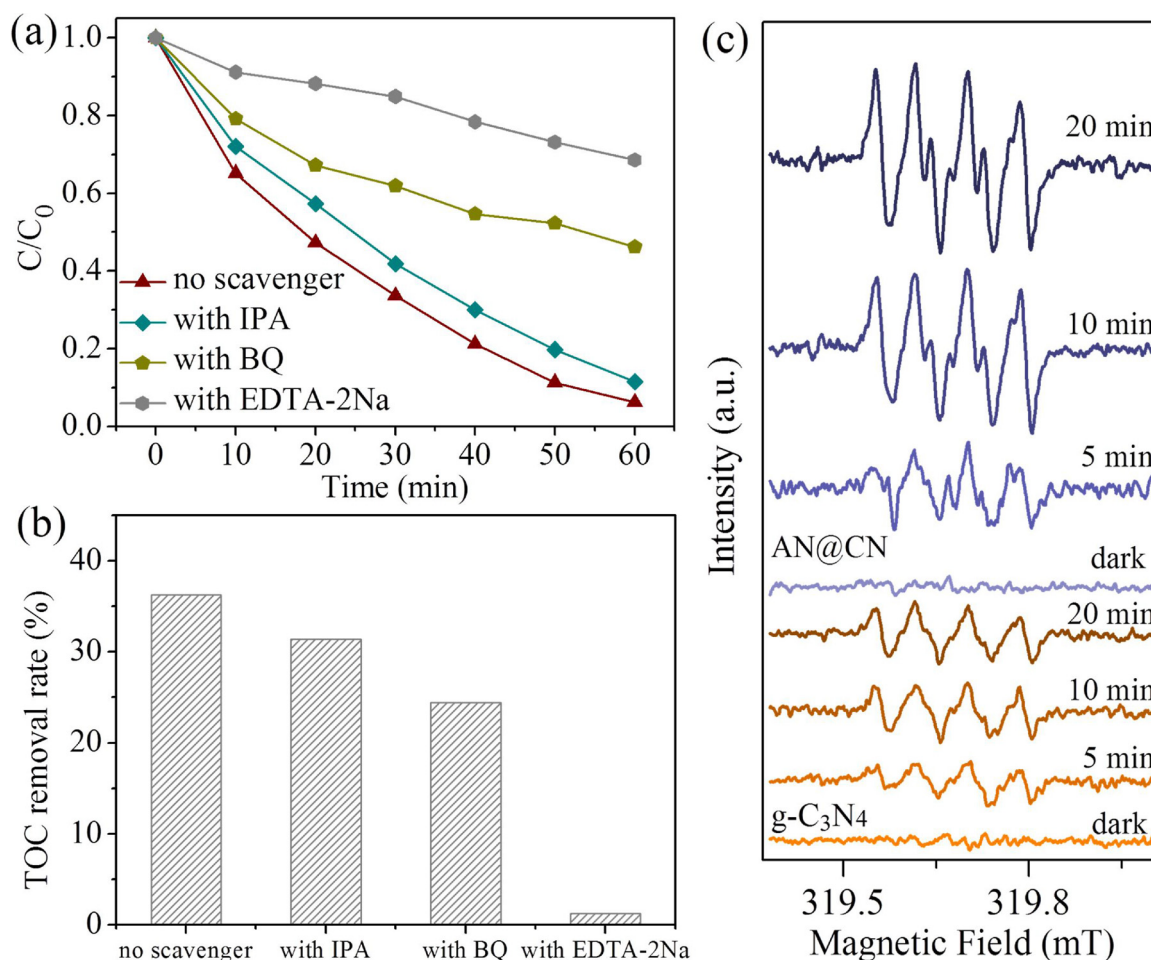
Fig. 7. (a) The DC degradation and (b) TOC removal efficiency of AN@CN catalysts with different scavengers under visible light irradiation. (c) ESR signals of DMPO-O_2^- adducts in the presence of g-C_3N_4 and AN@CN under visible light irradiation.

potential CB to the low potential one, resulting in a decrease of reactivity. The enhanced reactivity of photoelectrons in AN@CN (revealed from the increased single intensity of DMPO-O_2^-) indicated the electron transfer was not from g-C_3N_4 to Ag_2CrO_4. A Z-scheme transfer process could be proposed to the AN@CN photocatalysts, which was consistent with the previous XPS analysis results.

Therefore, a reasonable reaction mechanism of AN@CN could be proposed and illustrated in Scheme 2 . When exposed to the UV or visible light, both g-C_3N_4 and Ag_2CrO_4 could be excited and produce photogenerated electron-hole pairs. Since high-energy electrons tend to return to low potential positions, the excited photoelectrons usually return to the VB extremely quickly and recombine with holes to lose the reactive activity. With the formation of AN@CN heterojunction, the photoelectrons on the CB of Ag_2CrO_4 could shift to the VB of g-C_3N_4 under the drive of internal electric field, resulting in the accumulation of electrons and holes on the higher energy CB of g-C_3N_4 and VB of Ag_2CrO_4. The existence of N-GQDs could effectively enhance this Z-scheme electron transfer process. In this case, not only could the charge separation be enhanced, but also its high reactivity could be retained. The photoelectrons on the CB of g-C_3N_4 could transfer to the dissolved oxygen to form O_2^-. However, the holes on the VB of Ag_2CrO_4 do not have enough capacity to oxidize water into OH due to their finite potential (2.16 eV vs. NHE). The degradation process of DC was carried out under the synergistic effect of O_2^- and holes. DC could be damaged by O_2^- and holes to form a series of intermediate products, and the holes could continue to mineralize the intermediate products into CO_2 and H_2O. While under near-infrared light irradiation, the g-C_3N_4 and Ag_2CrO_4 could not be excited directly due to their limited absorbance,

but the N-GQDs in AN@CN could absorb near-infrared light and emit shorter wavelength light (425–520 nm) through a two-photon up-conversion PL process. Then the emitted visible light could excite g-C_3N_4 and Ag_2CrO_4 to generate electron-hole pairs for DC degradation.

4. Conclusion

In summary, the N-GQDs-containing AN@CN core-shell Z-scheme photocatalysts were prepared successfully and showed enhanced photocatalytic performance toward DC under full-spectrum light irradiation. The synergistic effects of the ternary combination of g-C_3N_4, Ag_2CrO_4 and N-GQDs significantly enhanced the optical absorption, charge separation and surface electron transfer efficiency of AN@CN photocatalysts. Due to the formation of Z-scheme transfer process under the promoting by N-GQDs, the photoelectrons excited on the Ag_2CrO_4 could shift to the g-C_3N_4 shell with inhibited photocorrosion, which endowed AN@CN with excellent stability. We believe that this strategy could provide a direction for improving the stability of materials suffered from photocorrosion and the preparation of photocatalysts with full-spectrum light response.
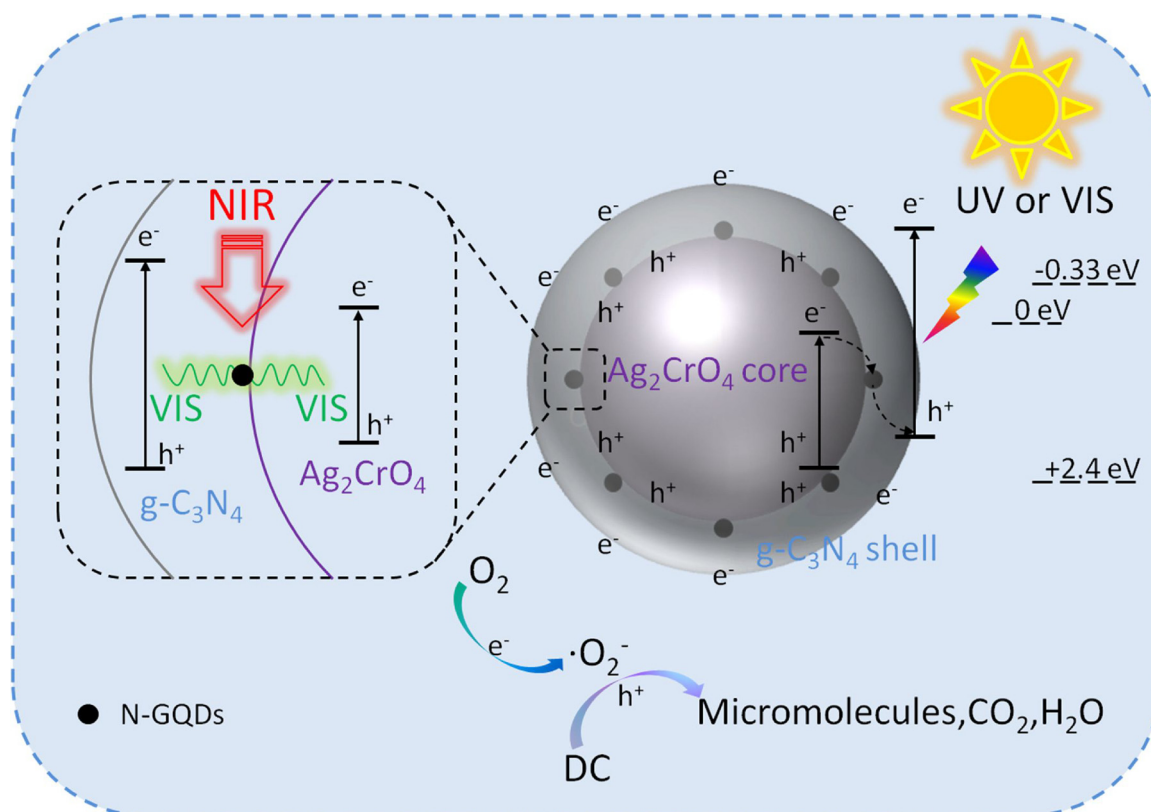
Scheme 2. Schematic diagram for the charge transfer and photocorrosion inhibition of AN@CN photocatalysts.

Appendix A. Supplementary data

Supplementary material related to this article can be found, in the online version, at doi:https://doi.org/10.1016/j.apcatb.2018.08.049.

References

[1] L. Tang, H. Feng, J. Tang, G. Zeng, Y. Deng, J. Wang, Y. Liu, Y. Zhou, Water Res. 117 (2017) 175–186.
[2] J.J. Wang, L. Tang, G. Zeng, Y. Liu, Y. Zhou, Y. Deng, J. Wang, B. Peng, ACS Sustain. Chem. Eng. 5 (2016) 1062–1072.
[3] L. Tang, J. Yu, Y. Pang, G. Zeng, Y. Deng, J. Wang, X. Ren, S. Ye, B. Peng, H. Feng, Chem. Eng. J. 336 (2018) 160–169.
[4] L. Tang, J. Wang, G. Zeng, Y. Liu, Y. Deng, Y. Zhou, J. Tang, J. Wang, Z. Guo, J. Hazard. Mater. 306 (2016) 295.
[5] J. Wang, L. Tang, G. Zeng, Y. Deng, Y. Liu, L. Wang, Y. Zhou, Z. Guo, J. Wang, C. Zhang, Appl. Catal. B-Environ. 209 (2017) 285–294.
[6] M. Zhu, S. Kim, L. Mao, M. Fujitsuka, J. Zhang, X. Wang, T. Majima, J. Am. Chem. Soc. 139 (2017) 13234.
[7] L. Mu, Y. Zhao, A. Li, S. Wang, Z. Wang, J. Yang, Y. Wang, T. Liu, R. Chen, J. Zhu, Energy Environ. Sci. 9 (2016).
[8] X. Jiao, Z. Chen, X. Li, Y. Sun, S. Gao, W. Yan, C. Wang, Q. Zhang, Y. Lin, Y. Luo, J. Am. Chem. Soc. 139 (2017) 7586.
[9] S. Wang, Y. Guan, L. Lu, Z. Shi, S. Yan, Z. Zou, Appl. Catal. B-Environ. 224 (2018) 10–16.
[10] D. Fang, J. Xie, D. Mei, Y. Zhang, F. He, X. Liu, Y. Li, RSC Adv. 4 (2014) 25540.
[11] D. Meng, Q. Xu, Y. Jiao, Y. Guo, Y. Guo, L. Wang, G. Lu, W. Zhan, Appl. Catal. B-Environ. 221 (2018) 652–663.
[12] S.K. Kim, H. Cho, M.J. Kim, H.J. Lee, J. Park, Y.B. Lee, H.C. Kim, W.Y. Chang, S.W. Nam, O.K. Sang, J. Mater. Chem. A 1 (2013) 1976–1981.
[13] X. Li, H. Ren, Z. Zou, J. Sun, J. Wang, Z. Liu, Chem. Commun. 52 (2015) 453.
[14] Y. Lin, S. Wu, X. Li, X. Wu, C. Yang, G. Zeng, Y. Peng, Q. Zhou, L. Lu, Appl. Catal. B-Environ. 227 (2018) 557–570.
[15] T. Zhang, M.-Y. Wu, D.-Y. Yan, J. Mao, H. Liu, W.-B. Hu, X.-W. Du, T. Ling, S.-Z. Qiao, Nano Energy 43 (2018) 103–109.
[16] S. Wang, B.Y. Guan, Y. Lu, X.W. Lou, J. Am. Chem. Soc. 139 (2017) 17305–17308.
[17] J. Ke, J. Liu, H. Sun, H. Zhang, X. Duan, P. Liang, X. Li, M.O. Tade, S. Liu, S. Wang, Appl. Catal. B-Environ. 200 (2017) 47–55.
[18] H. Tada, T. Mitsui, T. Kiyonaga, T. Akita, K. Tanaka, Nat. Mater. 5 (2006) 782.
[19] Y. Wang, X. Wang, M. Antonietti, Angew. Chem. Int. Edit. 51 (2012) 68–89.
[20] X. Wang, K. Maeda, A. Thomas, K. Takanabe, G. Xin, J.M. Carlsson, K. Domen, M. Antonietti, Nat. Mater. 8 (2009) 76–80.
[21] X. Wang, X. Chen, A. Thomas, X. Fu, M. Antonietti, Adv. Mater. 21 (2010) 1609–1612.
[22] W.J. Ong, L.L. Tan, Y.H. Ng, S.T. Yong, S.P. Chai, Chem. Rev. 116 (2016) 7159–7329.
[23] Y. Deng, L. Tang, G. Zeng, J. Wang, Y. Zhou, J. Wang, J. Tang, L. Wang, C. Feng, J. Colloid Interf. Sci. 509 (2018) 219–234.
[24] G. Liu, P. Niu, C. Sun, S.C. Smith, Z. Chen, G.Q. Lu, H.M. Cheng, J. Am. Chem. Soc. 132 (2010) 11642–11648.
[25] G. Zhang, M. Zhang, X. Ye, X. Qiu, S. Lin, X. Wang, Adv. Mater. 26 (2014) 805–809.
[26] Y. Deng, L. Tang, C. Feng, G. Zeng, Z. Chen, J. Wang, H. Feng, B. Peng, Y. Liu, Y. Zhou, Appl. Catal. B-Environ. 235 (2018) 225–237.
[27] D. Santamaríapérez, E. Bandiello, D. Errandonea, J. Ruizfuertes, O. Gomis, J.A. Sans, F.J. Manjón, P. Rodríguezhernández, A. Muñoz, J. Phys. Chem. C 117 (2013) 12239–12248.
[28] S. Ouyang, Z. Li, J. Phys. Chem. C 112 (2008) 3134–3141.
[29] Y. Deng, L. Tang, G. Zeng, J. Wang, Y. Zhou, J. Wang, J. Tang, Y. Liu, B. Peng, F. Chen, J. Mol. Catal. A-Chem. 421 (2016) 209–221.
[30] L. Huang, X. Hu, S. Yuan, H. Li, T. Yan, L. Shi, D. Zhang, Appl. Catal. B-Environ. 203 (2017) 778–788.
[31] M. Zhu, Y. Muhammad, P. Hu, B. Wang, Y. Wu, X. Sun, Z. Tong, Z. Zhao, Appl. Catal. B-Environ. 232 (2018) 182–193.
[32] C. Xue, H. An, X. Yan, J. Li, B. Yang, J. Wei, G. Yang, Nano Energy 39 (2017) 513–523.
[33] F. Cheng, H. Wang, X. Dong, Chem. Commun. 51 (2015) 7176–7179.
[34] J. Wang, Z. Yang, X. Gao, W. Yao, W. Wei, X. Chen, R. Zong, Y. Zhu, Appl. Catal. B-Environ. 217 (2017) 169–180.
[35] F. Wang, P. Chen, Y. Feng, Z. Xie, Y. Liu, Y. Su, Q. Zhang, Y. Wang, K. Yao, W. Lv, G. Liu, Appl. Catal. B-Environ. 207 (2017) 103–113.
[36] Y. Deng, L. Tang, C. Feng, G. Zeng, J. Wang, Y. Lu, Y. Liu, J. Yu, S. Chen, Y. Zhou, Acs Appl. Mater. Inter. 9 (2017) 42816–42828.
[37] J. Zhang, Y. Guo, Y. Xiong, D. Zhou, S. Dong, J. Catal. 356 (2017) 1–13.
[38] Q. Liu, B. Guo, Z. Rao, B. Zhang, J.R. Gong, Nano Lett. 13 (2013) 2436–2441.
[39] R. Shi, Z. Li, H. Yu, L. Shang, C. Zhou, G.I.N. Waterhouse, L.Z. Wu, T. Zhang, Chemsuschem 10 (2017) 4650–4656.
[40] J. Wang, L. Tang, G. Zeng, Y. Deng, H. Dong, Y. Liu, L. Wang, B. Peng, C. Zhang, F. Chen, Appl. Catal. B-Environ. 222 (2018) 115–123.
[41] G. Zhang, G. Li, Z.A. Lan, L. Lin, A. Savateev, T. Heil, S. Zafeiratos, X. Wang, M. Antonietti, Angew. Chem. Int. Edit. 56 (2017) 13445–13449.
[42] S. Yang, Y. Gong, J. Zhang, L. Zhan, L. Ma, Z. Fang, R. Vajtai, X. Wang, P.M. Ajayan,

Adv. Mater. 25 (2013) 2452–2456.

[43] X. She, H. Xu, Y. Xu, J. Yan, J. Xia, L. Xu, Y. Song, Y. Jiang, Q. Zhang, H. Li, J. Mater. Chem. A. 2 (2014) 2563–2570.

[44] Y. Deng, L. Tang, G. Zeng, Z. Zhu, M. Yan, Y. Zhou, J. Wang, Y. Liu, J. Wang, Appl. Catal. B-Environ. 203 (2017) 343–354.

[45] Z. Zhang, J. Huang, M. Zhang, Q. Yuan, B. Dong, Appl. Catal. B-Environ. 163 (2015) 298–305.

[46] X.H. Li, H.Y. Xu, X.T. Zhang, Y.C. Liu, J.W. Sun, Y.M. Lu, Appl. Phys. Lett. 95 (2009) 42.

[47] Z. Zhang, K. Liu, Z. Feng, Y. Bao, B. Dong, Sci. Rep. 6 (2016) 19221.

[48] X. Xin, J. Lang, T. Wang, Y. Su, Y. Zhao, X. Wang, Appl. Catal. B-Environ. 181 (2016) 197–209.

[49] L. Tang, C. Feng, Y. Deng, G. Zeng, J. Wang, Y. Liu, H. Feng, J. Wang, Appl. Catal. B-Environ. 230 (2018) 102–114.

[50] D. Xu, S. Cao, J. Zhang, B. Cheng, J. Yu, Beilstein. J. Nanotech. 5 (2014) 658–666.

[51] Y. Gong, X. Quan, H. Yu, S. Chen, Appl. Catal. B-Environ. 219 (2017) 439–449.

[52] Y. Shang, X. Chen, W. Liu, P. Tan, H. Chen, L. Wu, C. Ma, X. Xiong, J. Pan, Appl. Catal. B-Environ. 204 (2017) 78–88.

[53] B. Xu, P. He, H. Liu, P. Wang, G. Zhou, X. Wang, Angew. Chem. Int. Edit. 53 (2014) 2339–2343.

[54] A. Fattah-Alhosseini, Arab. J. Chem. 9 (2016) S1342–S1348.

[55] Y. Bi, S. Ouyang, N. Umezawa, J. Cao, J. Ye, J. Am. Chem. Soc. 133 (2011) 6490–6492.

[56] J.L. Li, H.C. Bao, X.L. Hou, L. Sun, X.G. Wang, M. Gu, Angew. Chem. Int. Edit. 124 (2012) 1866–1870.

[57] V. Lebret, L. Raehm, J.O. Durand, M. Smaïhi, C. Gérardin, N. Nerambourg, M.H.V. Werts, M. Blancharddesce, Chem. Mater. 20 (2008) 2174–2183.

[58] W. Jiang, X. Zong, L. An, S. Hua, X. Miao, S. Luan, Y. Wen, F.F. Tao, Z. Sun, ACS Catal. 8 (2018) 2209–2217.

[59] G. Liu, J. Shi, F. Zhang, Z. Chen, J. Han, C. Ding, S. Chen, Z. Wang, H. Han, C. Li, Angew. Chem. Int. Edit. 53 (2014) 7295.

[60] J.C. Hill, A.T. Landers, J.A. Switzer, Nat. Mater. 14 (2015) 1150.

[61] B.A. Nail, J.M. Fields, J. Zhao, J. Wang, M.J. Greaney, R.L. Brutchey, F.E. Osterloh, ACS Nano 9 (2015) 5135.

[62] C. Liu, H. Huang, L. Ye, S. Yu, N. Tian, X. Du, T. Zhang, Y. Zhang, Nano Energy 41 (2017) 738–748.